

# Adaptive SIF-EKF Estimation for Fault Detection in Attitude Control Experiments

Alex McCafferty-Leroux<sup>a</sup>, Waleed Hilal<sup>a</sup>, S. Andrew Gadsden<sup>a</sup>, and Mohammad Al-Shabi<sup>b</sup>

<sup>a</sup>McMaster University, Hamilton, Canada

<sup>b</sup>University of Sharjah, Sharjah, United Arab Emirates

## ABSTRACT

An inherent property of dynamic systems with real applications is their high degree of variability, manifesting itself in ways that are often harmful to system stability and performance. External disturbances, modeling error, and faulty components must be accounted for, either in the system design, or algorithmically through estimation and control methods. In orbital satellite systems, the ability to compensate for uncertainty and detect faults is vital. Satellites are responsible for many essential operations on Earth, including GPS tracking, radio communication/broadcasting, defense, and climate monitoring. They are also expensive to design and fabricate, to deploy, and currently impossible to fix if suddenly inoperable. In being subjected to unforeseen disturbances or minor system failures, communications with Earth can cease and valuable data can be lost. Researchers have been developing robust estimation and control strategies for several decades to mitigate the effects of these failure modes. For instance, fault detection methods can be employed in satellites to detect deviations in attitude or actuator states such that error or incorrect data does not propagate further across its long life cycle. The Kalman Filter (KF) is an optimal state estimation strategy with sub-optimal nonlinear variations, commonly applied in most dynamic systems, including satellites. However, in the presence of aforementioned uncertainties, these optimal estimators tend to degrade drastically in performance, and must be replaced for more robust methods. The newly developed sliding-innovation filter (SIF) is one such candidate, as it has been demonstrated to perform state estimation robustly in faulty systems. Using an in-lab Nanosatellite Attitude Control Simulator (NACS), an adaptive hybrid formulation of the SIF and EKF is applied to a satellite system to detect faults and disturbances in experiments, based on the normalized innovation squares (NIS) metric. This strategy was demonstrated to improve state estimation accuracy in the presence of multiple faults, compared to conventional methods.

**Keywords:** Estimation theory, Kalman filter, Sliding Innovation Filter, optimal estimation, robust estimation, adaptive estimation, machine learning, CubeSat

## 1. INTRODUCTION

Satellites and spacecraft are reliant on their attitude control and determination system (ADCS) to perform essential operations. Unifying control and estimation/determination strategies, with this system they are able to maintain attitude accurately and under the influence of minor disturbances. Modern satellites have a wide variety of applications and constraints, some requiring short-term sub micro-radian accuracy and stability within  $10^{-4}$  deg/s.<sup>1,2</sup> Responsible for GPS tracking, communication/broadcasting, defense, and scientific observation, orbital satellites rely on the functionality and accuracy of the ADCS (among other systems), otherwise valuable data or services can be lost.

The causes of satellite failures exist on a broad spectrum and occur often. An analysis from S.A. Jacklin<sup>3</sup> determined that the failure rate of deployed small satellites from 2000 to 2016 was as high as 41.3%. These events, known commonly as satellite anomalies, can exist as temporary outages, complete and instant failure, or slow degradation over time.<sup>4</sup> Sensor degradation, for instance, presents significant issues for estimation and

---

Further author information: (Send correspondence to A. McCafferty-Leroux or S. A. Gadsden)

A.M.L.: E-mail: mccafler@mcmaster.ca

S.A.G.: E-mail: gadsden@mcmaster.ca

control, imposing noise or bias in measurements. Factors that have been known to be the cause of such effects are mostly environmental, discussed extensively by Bedingfield *et al.*<sup>5</sup> Ambient charged particles, electromagnetic interference (EMI), cosmic rays,<sup>6</sup> or object collision<sup>7–9</sup> are examples of these environmental disturbances. Human interaction factors, such as command error<sup>10</sup> or cyber-attacks,<sup>11</sup> are also prevalent, resulting in unexpected behaviour. The Hubble Space Telescope (HST) is an example of how such issues can be avoided without correction, where it ceases operations while passing over a certain region of Earth that induces high-energy particle background (South Atlantic Anomaly, SAA), causing its sensors to fault.<sup>12</sup> Sensor faults can result in situations like the failure of India’s Small Satellite Launch Vehicle (SSLV) rocket, where high frequency vibrations caused accelerometers to saturate and satellites to be deployed incorrectly.<sup>13</sup>

In the case of sensor degradation, or system upset due to failures or debris, robust estimation algorithms must be employed to mitigate significant errors and prevent failures. More conventional methods in nonlinear system state estimation, such as the extended Kalman filter (EKF) or unscented Kalman filter (UKF), produce near-optimal solutions but typically lack in robustness facing these issues. Failure to provide sufficient knowledge of the system can have further detrimental effects on the system, especially in high-precision applications. Though sub-optimal, robust estimation strategies can guarantee performance with bounded uncertainties.<sup>14</sup> Popular strategies in target tracking include  $H_\infty$  methods,<sup>15</sup> or hybridized frameworks with the UKF or particle filters (PF).<sup>16,17</sup> The literature surrounding this field is numerous, having been extensively researched.

The smooth variable structure filter (SVSF) is one such method introduced by Habibi,<sup>18</sup> based on variable structure systems theory and sliding mode observers (SMOs).<sup>19</sup> Like the SMO, the SVSF is a recursive predictor-corrector estimator that utilizes discontinuity hyperplanes and an alternative gain formulation. The gain is calculated based on the estimation error and a switching term, which stabilizes the estimation process and bounds estimates.<sup>20</sup> The SVSF has since been modified for improvement in reducing chattering,<sup>21</sup> including a state error covariance,<sup>22</sup> higher-order formulations,<sup>23</sup> and fault detection.<sup>24</sup> For SVSF applications of fault-robust estimation and detection, an adaptive approach was implemented where the KF was applied in non-faulty situations, and the robust SVSF when a fault occurred.<sup>24,25</sup> The switching mechanisms applied to determine whether a fault occurred were the variable boundary layer (VBL) and the normalized innovation squares (NIS) methods. A recent alternative to the SVSF is the sliding innovation filter (SIF), which applies similar principals to the SVSF, utilizing a simpler gain formulation that resulted in higher accuracy.<sup>20</sup> Augmentations for nonlinear systems also exist, the most common of them the extended SIF (ESIF).<sup>20</sup> Among the many notable extensions of the SIF,<sup>26–28</sup> Hilal *et al.*<sup>29</sup> implement the SIF in the same manner as<sup>24</sup> for adaptive linear filtering based on the NIS metric, which has been shown to eliminate the effects of chattering by the VBL-based SVSF.

Of the following publication, the main contributions are as follows:

1. The ideas of Goodman and Hilal<sup>24,29</sup> are expanded on, extending their adaptive NIS-based filtering strategy to nonlinear systems.
2. The Nanosatellite Attitude Control Simulator (NACS) is used to validate the proposed design via laboratory experiment with data obtained across multiple fault trials.
3. The adaptive EKF-ESIF is applied for fault detection and robust state estimation in a simple satellite attitude tracking control scenario with comparison to conventional methods.

The remainder of this paper is organized as follows. Section 2 derives the satellite system model and Section 3 the proposed estimation strategy. Section 4 defines the parameters of the system and methodology of the experiment. Section 5 discusses the results of the experiment, and Section 6 provides conclusions and suggestions for future research.

## 2. SATELLITE MODEL DERIVATION

The satellite is modelled as a three rotational degree of freedom rigid body, considering the body frame  $B$  with respect to the North-East-Down (NED) inertial frame  $I$ , as the convention of,<sup>30</sup> denoted  $BI$ . This relationship is represented in Figure 1. The following section derives attitude kinematics and dynamics based on angular momentum  $\mathbf{H}(t)$ , along with the actuator dynamics related to the control input  $\mathbf{u}(t)$ . Vectors are time-varying,  $t$  for  $t \geq 0$ .

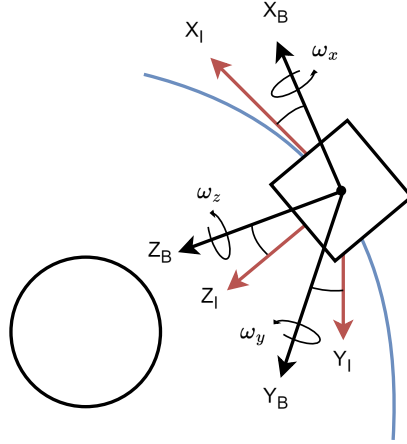


Figure 1: Orbital Satellite Diagram

## 2.1 Satellite Attitude Kinematics

The quaternion  $\mathbf{q}(t) \in \mathbb{R}^4$  is utilized to express the satellite attitude without singularities or trigonometric functions. The attitude matrix is expressible as a homogeneous quadratic function of its elements in this manner,<sup>30</sup> where the quaternion identity is expressed as  $\mathbf{q}_I = [0 \ 0 \ 0 \ 1]^T$ . The quaternion derivative is presented as Equation 1.

$$\dot{\mathbf{q}}_{BI}(t) = \frac{1}{2} [\omega_B^{BI} \otimes] \mathbf{q}_{BI}(t) \quad (1)$$

Where  $\omega(t) \in \mathbb{R}^3$  is the angular velocity of the satellite body. The skew symmetric matrices required for preserving the quaternion norm are also defined in Equations 2 and 3.

$$[\omega_B^{BI} \otimes] = \begin{bmatrix} -[\omega \times] & \omega(t) \\ -\omega(t)^T & 0 \end{bmatrix} \quad (2)$$

$$[\omega \times] = \begin{bmatrix} 0 & -\omega_z(t) & \omega_y(t) \\ \omega_z(t) & 0 & -\omega_x(t) \\ -\omega_y(t) & \omega_x(t) & 0 \end{bmatrix} \quad (3)$$

## 2.2 Satellite Attitude Dynamics

The dynamics of the body due to inertial and applied forces are derived based on the net angular momentum  $\mathbf{H}(t) \in \mathbb{R}^3$ , producing the rate of change equation for  $\omega(t)$ . The net momenta around the center of mass (CoM)  $c$  is generally represented as Equation 4. From this, its time derivative is also computed in the following forms, presented in Equation 5.

$$\mathbf{H}_B^c(t) = J_B^c \omega_B^{BI}(t) \quad (4)$$

$$\dot{\mathbf{H}}_B^c(t) = \mathbf{L}_B^c(t) - \omega_B^{BI}(t) \times \mathbf{H}_B^c(t) = J_B^c \dot{\omega}_B^{BI}(t) \quad (5)$$

Where  $\mathbf{L}_B^c(t) \in \mathbb{R}^3$  are the internal and external torques acting on the satellite. The total moment of inertia (MOI) matrix of the satellite is constant and expressed as  $J_B^c \in \mathbb{R}^{3 \times 3}$ . The satellite under study is based on the lab experimental setup previously mentioned, the NACS. The setup uses a reaction wheel (RW) configuration for actuation, oriented in the pyramidal arrangement (see Figure 2).

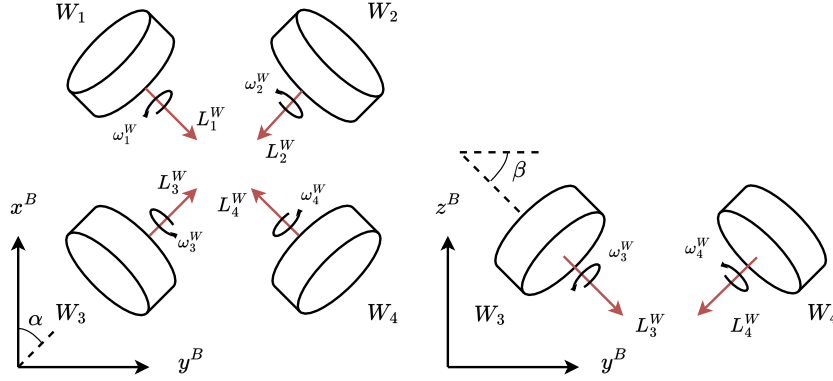


Figure 2: Reaction Wheel Actuator Frame Representation (**Left:** Top View, **Right:** Side View)

The velocity of the RW actuator (RWA) in the wheel frame  $W$  is represented as  $\omega_W^W(t) \in \mathbb{R}^4$ . To map each respective wheel frame to the body frame  $B$ , the constant matrix  $W_4 \in \mathbb{R}^{3 \times 4}$  is applied, where  $N \in \mathbb{Z}^+$ , corresponding to the number of RWs. The general equation for  $W_4$  is defined in Equation 6, where for the setup,  $\alpha = \beta = 45^\circ$ .

$$W_4 = \begin{bmatrix} \cos \alpha \cos \beta & \cos \alpha \cos \beta & -\cos \alpha \cos \beta & -\cos \alpha \cos \beta \\ -\sin \alpha \cos \beta & \sin \alpha \cos \beta & -\sin \alpha \cos \beta & \sin \alpha \cos \beta \\ -\sin \beta & -\sin \beta & -\sin \beta & -\sin \beta \end{bmatrix} \quad (6)$$

This relationship is expressed in Figure 2. The column elements of  $W_4$  are the unit orientations of each wheel and must satisfy unity magnitude.<sup>30</sup> As a rotating mass, the RWs therefore have their own momentum contribution  $\mathbf{H}(t)^W \in \mathbb{R}^4$ , which augments Equation 4 as Equations 7 and 8.

$$\mathbf{H}_B^c(t) = \mathbf{H}_B^B(t) + \mathbf{H}_B^W(t) = \mathbf{H}_B^B(t) + W_4 \mathbf{H}_W^W(t) \quad (7)$$

$$\mathbf{H}_B^c(t) = J_B \omega_B^{\text{BI}}(t) + W_4 J_W^W \omega_W^W(t) \quad (8)$$

As previously mentioned, the net torque  $\mathbf{L}_B^c(t)$  has external and internal components. The external component  $\mathbf{L}_B(t) \in \mathbb{R}^3$  is representative of some disturbance, such as gravity gradient or aerodynamic forces in low Earth orbit (LEO). In the lab environment, lacking certain equipment, this is generalized as small process noise. The internal torque  $\mathbf{L}_W(t) \in \mathbb{R}^4$  is generated due to the rate of momentum of the wheels (i.e., torque is generated in acceleration). Since the actuators are controllable,  $\mathbf{L}_W(t)$  is transformed with  $W_4$  into the body frame, and alternatively represented as  $\mathbf{u}(t) \in \mathbb{R}^3$ , the common convention for control input. The separation of  $\mathbf{L}_B^c(t)$  is substituted into Equation 5, and then 8, where the satellite attitude dynamics are derived as Equation 9.

$$\dot{\omega}_B^{\text{BI}}(t) = (J_B)^{-1} [\mathbf{L}_B(t) - \mathbf{u}(t) - \omega_B^{\text{BI}}(t) \times (J_B \omega_B^{\text{BI}}(t) + W_4 J_W^W \omega_W^W(t))] \quad (9)$$

### 2.3 Reaction Wheel Dynamics

The rotational dynamics of the RWs are a function of the control torque  $\mathbf{u}(t)$ . Equation 5 in the frame  $W$  is expressed as Equation 10, where the relationship to the control torque on the body frame  $B$  is obtained with the pseudo-inverse of  $W_4$ .

$$\dot{\omega}_W^W(t) = J_W^{-1} \mathbf{L}_W(t) = J_W^{-1} W_4^+ \mathbf{u}(t) \quad (10)$$

The satellite system expressed by Equations 1, 9, and 10 can be generally represented by the nonlinear function  $\dot{\mathbf{x}}(t) = f(\mathbf{x}(t), \mathbf{u}(t))$ , or by its discrete form  $\mathbf{x}_{k+1} = f(\mathbf{x}_{k|k}, \mathbf{u}_k)$ . It is worth noting that the state vector is structured as  $\mathbf{x}(t) = [\mathbf{q}^B(t) \ \omega^B(t) \ \omega^W(t)]^T \in \mathbb{R}^n$ , where  $n = 11$ , and the control vector  $\mathbf{u}(t) \in \mathbb{R}^r$ , where  $r = 3$  corresponding to the principal axes of the body frame  $B$ .

### 3. ESTIMATION METHOD DERIVATION

#### 3.1 Extended Kalman Filter

The EKF is commonly applied in spacecraft as a predictor-corrector estimation strategy in nonlinear systems. A recursive process, the EKF predicts true states from the discrete model of the system in two stages: the *a priori* and *a posteriori*. The following section outlines the EKF process, the SIF, and the proposed EKF-SIF augmentation for fault detection.

The *a priori* is the first stage in estimation, using the nonlinear and linear approximations of the model to determine the state vector  $\hat{\mathbf{x}}_{k+1|k} \in \mathbb{R}^n$  and state error covariance  $P_{k+1|k} \in \mathbb{R}^{n \times n}$ . The *a priori* process is outlined in Equations 11 and 12 below.<sup>31</sup> The system and control matrices  $A_k$  and  $B_k$  that describe the linearized system are determined from the nonlinear equations via Jacobian and are time-varying. The system noise covariance is represented by  $Q_k \in \mathbb{R}^{n \times n}$ .

$$\hat{\mathbf{x}}_{k+1|k} = f(\hat{\mathbf{x}}_{k|k}, \mathbf{u}_k) \quad (11)$$

$$P_{k+1|k} = A_k P_{k|k} A_k^T + Q_k \quad (12)$$

The *a posteriori* equations are then applied to correct predictions, decreasing the estimation variance based on a measurement  $\mathbf{z}_{k+1} \in \mathbb{R}^m$ . Equations 13, 14, 15, and 16 are representative of this step.

$$S_{k+1} = C_{k+1} P_{k+1|k} C_{k+1}^T + R_{k+1} \quad (13)$$

$$K_{k+1} = P_{k+1|k} C_{k+1}^T S_{k+1}^{-1} \quad (14)$$

$$\hat{\mathbf{x}}_{k+1|k+1} = \hat{\mathbf{x}}_{k+1|k} + K_{k+1} (\mathbf{z}_{k+1} - C \hat{\mathbf{x}}_{k+1|k}) \quad (15)$$

$$P_{k+1|k+1} = (I - K_{k+1} C_{k+1}) P_{k+1|k} (I - K_{k+1} C_{k+1})^T + K_{k+1} R_{k+1} K_{k+1}^T \quad (16)$$

The corrected state and error covariances are defined  $\hat{\mathbf{x}}_{k+1|k+1}$  and  $P_{k+1|k+1}$ , respectively, with the innovation and measurement noise covariances,  $S_{k+1} \in \mathbb{R}^{m \times m}$  and  $R_{k+1} \in \mathbb{R}^{m \times m}$ . All system states are measurable for the application ( $n = m$ ), with  $C \in \mathbb{R}^{m \times n} = I_{n \times n}$ .

#### 3.2 Sliding Innovation Filter

The proposed fault detection method utilizes the extended SIF for robust state estimation.<sup>20</sup> The SIF follows the same predictor-corrector equations as the EKF (Equations 11 - 13, 15, 16), but modifies the gain of Equation 14. The correcting gain  $K_{k+1} \in \mathbb{R}^{n \times m}$  is derived primarily as a function of the innovation  $\tilde{\mathbf{z}}_{k+1|k} \in \mathbb{R}^m$  (Equation 17) and omits the state error covariance.

Featuring a switching mechanism, with the alternative gain the robustness of the state estimation of the system subjected to modeling error, disturbances, etc. is realized. The switching is achieved with the saturation function, keeping estimates enclosed within a defined constant boundary layer, denoted  $\delta \in \mathbb{R}^m$ , and forcing estimates to an existence subspace. Illustrated by Figure 3, this enables estimates to converge to the trajectory with minimal error. The SIF gain is then defined as Equation 18, as originally formulated in.<sup>20</sup>

$$\tilde{\mathbf{z}}_{k+1|k} = \mathbf{z}_{k+1} - C_{k+1} \hat{\mathbf{x}}_{k+1|k} \quad (17)$$

$$K_{k+1} = C^+ \text{sat}(|\tilde{\mathbf{z}}_{k+1|k}|/\delta) \quad (18)$$

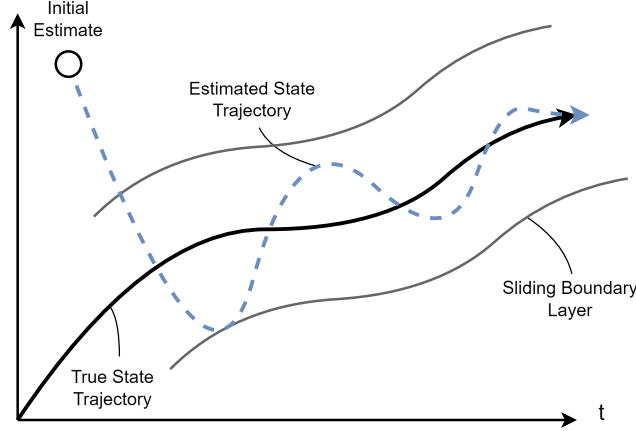


Figure 3: SIF Behaviour Illustration

### 3.3 EKF-SIF Hybrid Formulation

It was originally proposed by Goodman *et al.*<sup>24</sup> for the SVSF and by Lee *et al.*<sup>32</sup> for the SIF that the boundary layers of these respective filters can be made variable. Considering that the rate of change of the variable boundary layer (VBL) is formulated to be proportional to the absolute value of the innovation, under the presence of a fault the VBL will increase to a relatively large value. The fault can be detected from this mechanism, specifically when the VBL surpasses a predetermined threshold. Utilizing this method with the standard KF in non-faulty cases, a robust adaptive SIF-KF is applied. It was observed, however, that chattering can result from high-frequency switching between these two filters.<sup>24,29</sup> To address this issue in linear systems,<sup>24</sup> the NIS metric was applied to detect faults robustly without chattering. In this paper, it is proposed that the NIS-based SIF-KF be extended to nonlinear systems.

The EKF assumes a zero-mean Gaussian noise model with assumed covariances and the model defined in Section 2. In the presence of harmful faults, the EKF estimates will diverge from the measurements, increasing the innovation as a consequence. From Equation 19, it can be concluded that the NIS value will increase with the innovation, resulting in a fault detection mechanism from monitoring its state. Similar to the VBL case described above, the NIS-based method proposed as the NIS EKF-ESIF utilizes thresholding. Below the threshold, the EKF gain of Equation 14 is utilized and above the threshold, the ESIF gain of Equation 18 is utilized to estimate the system robustly. The NIS metric is defined as the time-varying parameter  $\mathbf{r}_k \in \mathbb{R}^1$ , Equation 19.

$$\mathbf{r}_k = \tilde{\mathbf{z}}_k^T S_k^{-1} \tilde{\mathbf{z}}_k \quad (19)$$

The NIS filter is optimal and matched, characterized by the chi-squared distribution with  $N$  degrees of freedom (DoF), where  $N$  is the number of measurements.<sup>29</sup> To avoid the occurrence of erratic switching about a single threshold, two thresholds are employed. Applying a hysteresis approach, false SIF triggers can be avoided with a higher "on" point and a lower "off" point is applied for switching when innovations are typical.<sup>29</sup> The gain applied when the NIS metric is between these two thresholds is therefore based on the most recent threshold crossed.

The robustness can also be improved if the history of the innovations is considered as opposed to each instance. The addition of this consideration will reduce the false triggering from anomalies that are not characterized as faults, such as noise.<sup>24,29</sup> Two methods can be considered for this application, the windowed average and fading memory approaches. These methods are applied for a comparative analysis in Section 5.

The windowed or moving average NIS,  $\mathbf{r}_k^w \in \mathbb{R}^1$  averages the innovations across a defined number of past sequences  $w \in \mathbb{R}^+$  from the current time step  $k$ . With  $k > w$ , the innovations that occurred before  $k - w + 1$  are not considered, having a finite consideration horizon. The windowed average NIS is determined from Equation 20.

$$\mathbf{r}_k^w = \sum_{j=k-w+1}^k \mathbf{r}_j \quad (20)$$

The fading memory NIS,  $\mathbf{r}_k^\alpha \in \mathbb{R}^1$  on the other hand considers the entire history of innovations. Utilizing a forgetting factor  $\alpha \in (0, 1)$ , more distant innovations from the current time step  $k$  are weighted exponentially lower.<sup>29</sup> The fading memory NIS is determined from Equation 21.

$$\mathbf{r}_k^\alpha = \alpha \mathbf{r}_{k-1}^\alpha + \mathbf{r}_k \quad (21)$$

The threshold values are defined based on the chi-squared distribution. Specifically, the DoF  $n$  and the significance/tail probability  $p$  are used to determine the critical value from a chi-squared table. The critical value is taken as the threshold (before switching modification), as this value signifies the threshold for statistical significance. For the windowed average, the chi-squared DoF is defined as Equation 22 and Equation 23 for the fading memory.<sup>33</sup>

$$\chi_{nw}^2 = wN \quad (22)$$

$$\chi_{n\alpha}^2 = \frac{N}{1 - \alpha} \quad (23)$$

#### 4. METHODOLOGY

To validate the fault detection method, the NACS will be utilized. A trajectory-tracking attitude control experiment will be performed under the specified scenarios, where faults are introduced artificially. The satellite simulator will actuate itself to follow sinusoidal attitude signals, simulating a moving target. The estimation strategies will be applied to the collected data afterward.

Required for estimation is a model of the system. For *a priori* estimation, the nonlinear system is applied, presented as Equation 24. The system is then linearized via Jacobian to obtain the time-varying system and control matrices,  $A_k$  and  $B_k$ . For completeness, the measurement equation is presented as Equation 25, where  $C$  is assumed to be constant identity.

$$\dot{\mathbf{x}}_k = \begin{bmatrix} \frac{1}{2} [\omega_k^B \otimes] \mathbf{q}_k \\ J_B^{-1} [\omega_k^B \times (J_B \omega_k^B + W_N J_W \omega_k^W)] \\ 0_{4 \times 11} \end{bmatrix} + \begin{bmatrix} 0_{4 \times 3} \\ -J_B^{-1} \\ J_W^{-1} W_N^+ \end{bmatrix} \mathbf{u}_k + \mathbf{w}_k \quad (24)$$

$$\mathbf{z}_k = C \mathbf{x}_k + \mathbf{v}_k \quad (25)$$

For the modeling, it is assumed that the simulator is balanced and the effect of gravity is minimal. The airflow past the air bearing to the automatic balancing system (ABS) plate is not modeled, though exists as small process noise. For filtering, the process and sensor noise is assumed to be sufficiently modeled with a zero-mean Gaussian process. The associated covariance matrices are defined in Section 5, experimentally determined.

The constant parameters of the simulator are the system and RW inertias,  $J^B$  and  $J^W$ , and the RW mapping.  $W_4$  can be determined utilizing Equation 6 and the provided  $\alpha$  and  $\beta$  values at  $45^\circ$ . It is assumed for modeling that the physical alignment of these actuators coincides with the pyramidal geometry. The inertias were determined from the Solidworks model as the following:

$$J_B = \begin{bmatrix} 0.021867 & -0.001532 & -0.000631 \\ -0.001532 & 0.172994 & -0.000781 \\ -0.000631 & -0.000781 & 0.0316484 \end{bmatrix} kg \ m^2 \quad (26)$$

$$J_W = 1.740138 \times 10^{-5} kg \ m^2$$

For the experiments, actuator and disturbance faults are applied to the system. In disabling one or more actuators, or reducing its operation efficiency, the performance of the system will be diminished as the satellite loses a significant portion of its controllability. Large disturbances can also result in unrecoverable tumbling. In Section 5, four experimental cases are presented for a variety of estimation methods, demonstrating the respective performance under fault-free, and various temporary fault scenarios. The EKF, ESIF, and proposed ESIF-EKF with the different NIS metrics are compared for experimental validation, where each experiment is performed 10 times to enhance the reliability of the results. For attitude control  $\mathbf{u}(t)$ , a proportional-derivative (PD) controller (Equation 27) is implemented, with experimentally determined gains of  $K_p = 0.4$  and  $K_d = 0.075$ .

$$\mathbf{u}(t) = -K_p \text{sign}(q_4(t)) \mathbf{q}_{1:3}(t) - K_d \boldsymbol{\omega}_B^{\text{BI}}(t) \quad (27)$$

The experiment runs for 1000 iterations, where the entire loop samples at approximately 0.1 seconds on average. The trajectory for the attitude tracking control scenario is governed by a time-varying quaternion with sinusoidal form, based on the initial condition. A sample of the trajectory is provided in Figure 4.

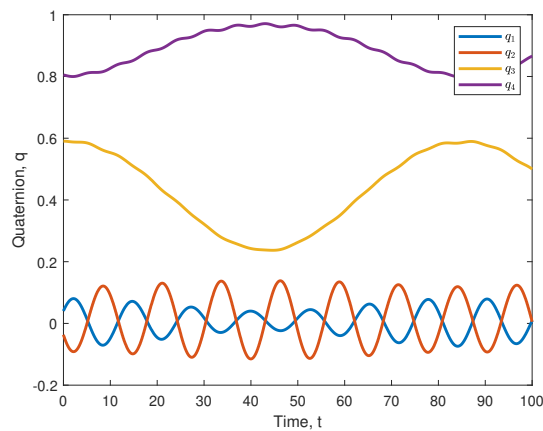


Figure 4: Desired Quaternion Trajectory

The NACS is presented in Figure 5, with the CubeSat and ABS units. The main components of the mock CubeSat unit are the RWAs, their respective ESCON motor drivers, the VN-100 inertial measurement unit (IMU), power supplies and onboard computer (OBC), and the motherboard. Control actions are computed on the Raspberry Pi 3A+ OBC. The ABS is fixed to the mock CubeSat, consisting of its translatable masses and associated control electronics, and a hemispherical air bearing. The pseudo 'zero-gravity' environment for satellite simulation is facilitated by the ABS, where the center of mass of the system can be automatically tuned to be coincident with the center of rotation of the air bearing, effectively nullifying gravitational forces. Note that for fault detection, the system had to be correctly balanced, otherwise the disturbance torque due to gravity would result in false triggers. As a consequence of geometry, the range of motion for the system is  $\pm 360^\circ$  in the yaw, and  $\pm 30^\circ$  in the pitch and roll. The air pressure for the bearing is regulated to 1 bar (approx. 14.5 psi) while running, tuned to be the minimum pressure without binding or excessive flow forces. Experiment operations are controllable with a graphical user interface (GUI).

## 5. EXPERIMENTAL RESULTS

To validate the proposed hybrid EKF-ESIF method with NIS-based gain switching, the performance is compared to the EKF and SIF. The two methods of NIS calculation described in Section 3.3, windowed average and fading memory, are compared as well. The filters will be evaluated in four experiment cases: no fault, disturbance fault, temporary RWA effectiveness loss, and temporary RWA failure. For analysis, the root mean squared error (RMSE) of the attitude states ( $\mathbf{q}$  and  $\boldsymbol{\omega}$ ) is individually presented, along with the sum of all RMSE. The RMSE data is averaged across 10 data sets for each of the four cases.

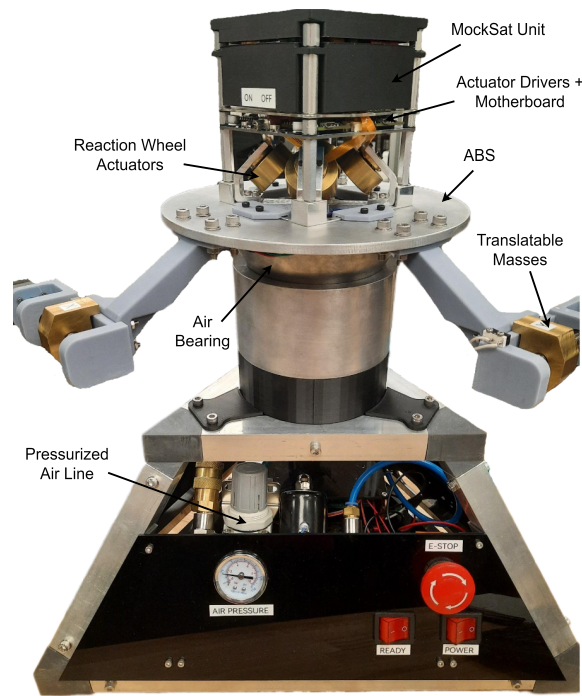


Figure 5: Nanosatellite Attitude Control Simulator

For the fault-free case, the CubeSat unit tracks the trajectory of Figure 4 with minimal disturbance. Excess disturbances are due to process noise and a small imbalance in the system. It is important in selecting NIS thresholds and the system noise covariance  $Q$  that normal operation is established correctly and does not trigger switching due to a detected fault. For the disturbance case, one or more planar disturbances are applied to the system part-way through the experiment. Due to the geometry of the simulator, the disturbances are bounded in their resultant displacement. The temporary loss of effectiveness of all actuators is considered next, where the commanded RW torque is 75% less than was calculated from the control law. This fault occurs between iteration 200 and 400 of the simulation. The RW failure case considers the complete loss of power to a single actuator, from iteration 200 to 600.

The measurement noise covariance matrix  $R$  was assumed constant, where its diagonal entries were estimated to be the variance values reported in the VN-100 IMU and ESCON 24/2 data sheets. For the quaternion and body angular velocity, the gyroscope variance values of  $3 \times 10^{-6} \text{ rad}^2/\text{s}^2$  were implemented, and for the RWA velocity, the output voltage variance of  $2.42 \times 10^{-3} \text{ V}$  was applied. In choosing  $Q$ , a trial and error method was applied, as it related to the overall magnitude of NIS values. For instance, with smaller  $Q$  entries, the NIS intensity was far higher than the alternative, due to high reliance on the model and minimal process noise expectancy. A constant diagonal  $Q$  with identical entries of  $4 \times 10^{-5}$  was selected. The boundary layer of the SIF was chosen through trial and error to have constant entries of  $\delta_{1:4} = 0.0004$ ,  $\delta_{5:7} = 0.008$ , and  $\delta_{8:11} = 0.02$ .

The tail probabilities for the on and off thresholds were chosen to be 0.001 and 0.05, respectively. For the windowed average, the window size  $w$  was chosen as 45 and the fading memory coefficient  $\alpha$  was selected as 0.965, giving preference to past NIS values. These parameters were tuned to consider past measurements and provided sufficient smoothing of typically stochastic NIS values. With a measurement size of 11, the DoF of the chi-squared value and the associated critical point can be evaluated with Equations 20 and 21.

## 5.1 No Fault

The results of the fault free case are presented in Table 1, along with sample NIS plots of each hybrid method as Figure 6. The NIS values are plotted on top, where the dotted orange represents the standard NIS and the solid blue is the smoothed NIS. The fault state is plotted below, where a '0' signifies no fault and a '1' is a fault.

For the fault free case, the EKF achieves the best overall estimation accuracy, where the system is adhering to the expected behaviour of the model with stochasticity. From Table 1, since no faults were detected, the NIS EKF-ESIF achieves essentially the same error results. Small deviations due to imbalance in the system generating a small torque at inclinations was observed in some data sets, creating a brief false fault event. Otherwise, the results should theoretically be exactly the same and the false triggers at small scales do not significantly deteriorate the performance. The windowed average NIS exhibited the false fault more often than the fading memory. The NIS thresholds were calibrated based on the fault free performance. No significant difference was observed between the results of the two NIS smoothing methods, since no true faults were present. As expected, the sub-optimal SIF exhibited the poorest performance in this case.

Table 1: Fault Free Case

RMSE $\times 10^{-3}$	EKF	SIF	WA NIS	FM NIS
$q_1$	0.01749	0.06840	0.02204	0.01954
$q_2$	0.02863	0.05824	0.03122	0.02973
$q_3$	0.01743	0.06949	0.02172	0.01895
$q_4$	0.00892	0.05995	0.01598	0.01232
$\omega_1$	0.59486	1.21634	0.63080	0.59702
$\omega_2$	0.47755	1.24777	0.52556	0.50529
$\omega_3$	0.66156	1.24744	0.67281	0.64219
$\Sigma_{RMSE}$	<b>1.80643</b>	<b>3.96762</b>	<b>1.92013</b>	<b>1.82504</b>

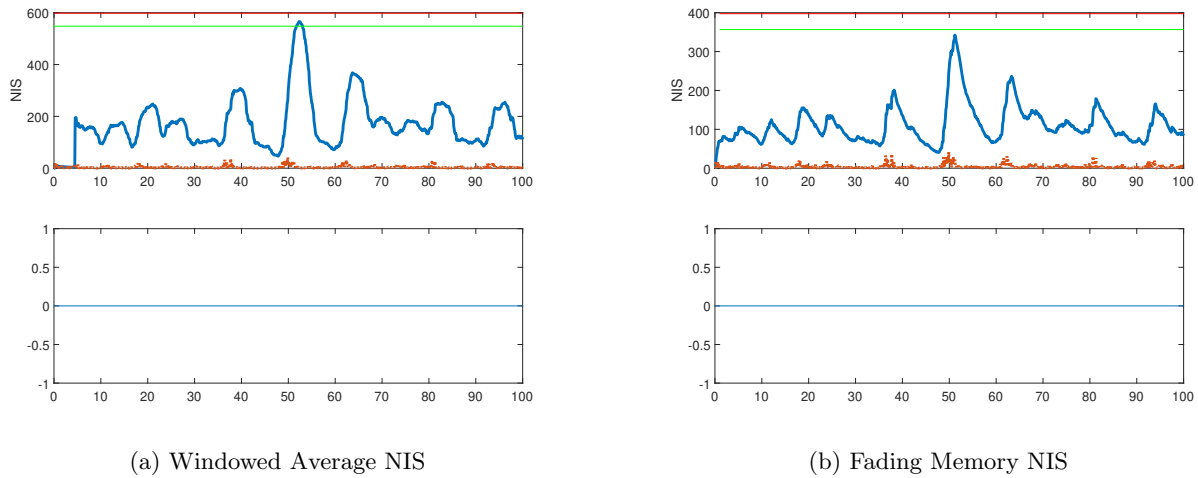


Figure 6: Sample NIS Plots for Hybrid EKF-SIF in Fault-Free Case

## 5.2 Disturbance Fault

The results of the disturbance case is presented in Table 2, along with sample NIS plots of each hybrid method as Figure 7. For the disturbance case, one or more planar disturbances of variable magnitude were temporarily applied to the system. It was observed that with the relatively large faults of Figure 7, the EKF had the worst performance overall, which was expected as a non-robust estimation method. The SIF performed the next best,

Table 2: Disturbance Fault Case

RMSE $\times 10^{-3}$	EKF	SIF	WA NIS	FM NIS
$q_1$	0.05302	0.06325	0.03077	0.03268
$q_2$	0.07430	0.05415	0.03763	0.03749
$q_3$	0.02638	0.06522	0.03601	0.03768
$q_4$	0.01685	0.06071	0.03719	0.03877
$\omega_1$	1.55941	1.09099	0.66113	0.64653
$\omega_2$	2.22498	1.13685	0.74969	0.63434
$\omega_3$	1.17942	1.13987	0.70874	0.70401
$\Sigma_{RMSE}$	<b>5.13437</b>	<b>3.61104</b>	<b>2.26117</b>	<b>2.13152</b>

accounting for the fault well, but still featured higher errors due to its constant sub-optimal estimation when the system was not recovering from the disturbance. The NIS EKF-ESIF methods result in the best performance, able to detect the fault and switch to the SIF gain, and switch back to the more optimal gain when the system recovered. It was observed throughout trials that the fading memory NIS computation resulted in the faulty state lasting longer than the NIS with the windowed average. This can be observed in Figure 6 and 7. In having steeper drops, more switching between modes occurs. Choosing a lower window length  $w$  would exacerbate this, where the NIS stochasticity is more prevalent with smaller values. Choosing larger windows was found to generally result in better smoothing. The activation of both method's fault modes are near instant and the same.

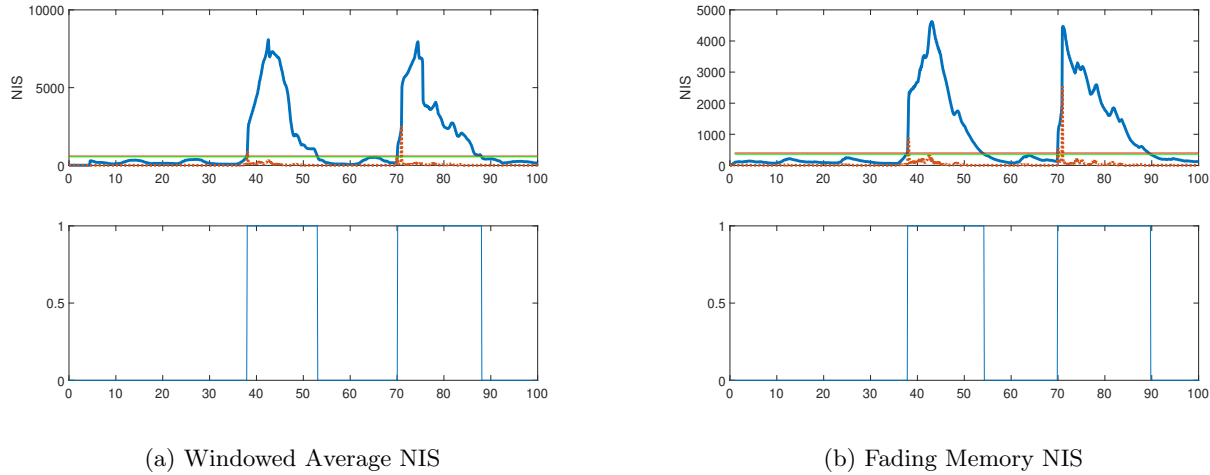


Figure 7: Sample NIS Plots for Hybrid EKF-SIF in Disturbance Case

### 5.3 Temporary Reaction Wheel Effectiveness Loss

The results of the RW effectiveness loss case is presented in Table 3, along with sample NIS plots of each hybrid method as Figure 8. In this case, the effectiveness of the RWAs were reduced to 25% for a short period of time. Though these faults were detectable from the NIS method, the effect it had on the system was comparatively smaller than the previous case studied. As such, the robust benefits of the SIF were not as desirable in terms of estimation accuracy, as can be noted from the results. It should be noted, however, that the RMSE of the state with SIF would be lower than the EKF, only for the fault time window. This specific interaction was studied in.<sup>29</sup> Compared overall, the EKF produced improved RMSE results over the SIF. Considering the NIS EKF-ESIF methods, the windowed average method performed slightly worse than that of the fading memory, which performed the best overall. Though the fault was constant from 20 seconds to 60 seconds, both detection methods had a delay in detection of approximately 5 seconds while the effect on the system was realized,

Table 3: Reaction Wheel Effectiveness Loss Fault Case

RMSE $\times 10^{-3}$	EKF	SIF	WA NIS	FM NIS
$q_1$	0.01954	0.04722	0.02687	0.02577
$q_2$	0.03011	0.03829	0.03487	0.03406
$q_3$	0.02126	0.04730	0.03050	0.02838
$q_4$	0.00967	0.04478	0.02657	0.02519
$\omega_1$	0.76460	0.96752	0.71342	0.65819
$\omega_2$	0.55215	1.00077	0.66519	0.64944
$\omega_3$	0.91856	0.98221	0.81572	0.73432
$\Sigma_{RMSE}$	<b>2.31590</b>	<b>3.12809</b>	<b>2.31314</b>	<b>2.15534</b>

as seen in Figure 8. The fault as additionally not registered for the full period of time consistently, having numerous intermediate switching events. This could be addressed though adjusting the thresholds or increasing the smoothing parameters, which would likely result in surpassing EKF performance.

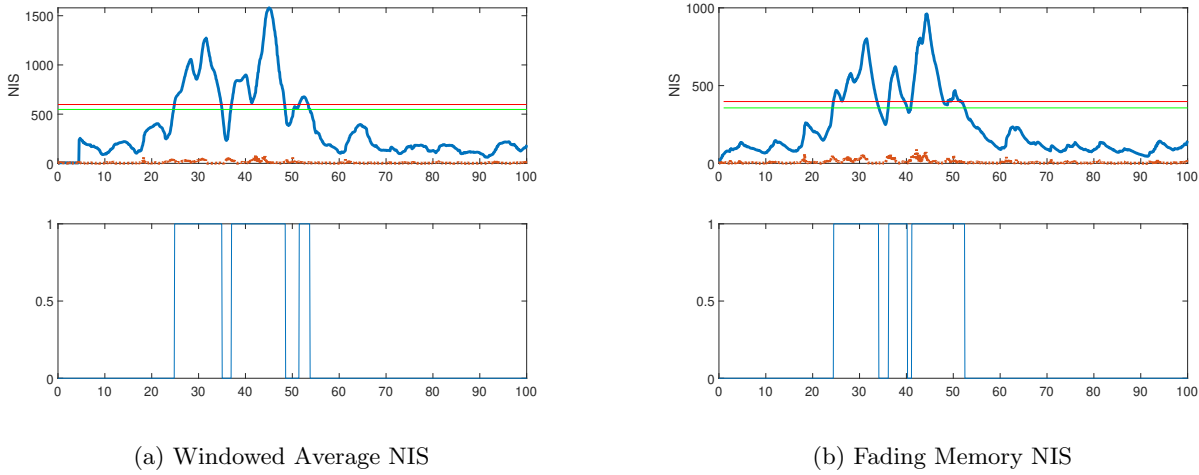


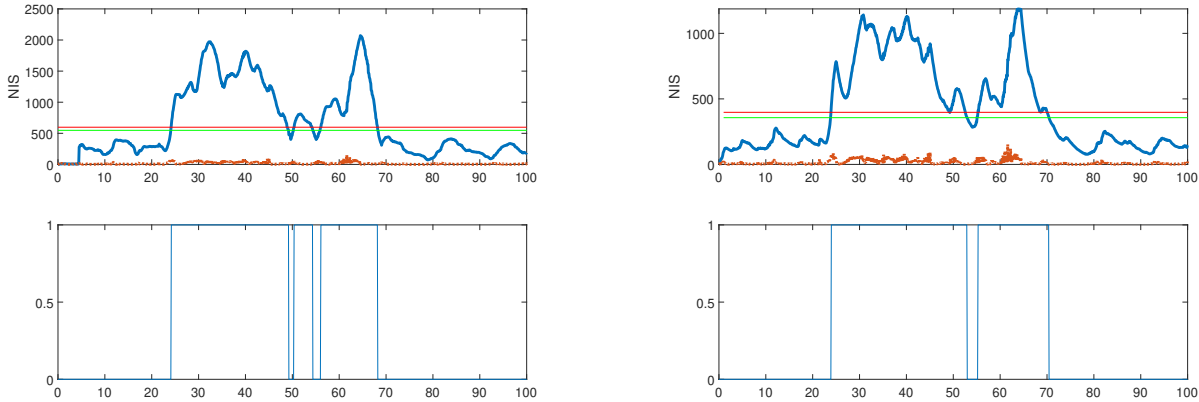
Figure 8: Sample NIS Plots for Hybrid EKF-SIF in Reaction Wheel Effectiveness Loss Case

#### 5.4 Temporary Reaction Wheel Failure

The results of the RW failure case is presented in Table 4, along with sample NIS plots of each hybrid method as Figure 9. The effects of the failure of a single RW are more prevalent than the effectiveness loss, resulting in generally higher NIS values. In the failure of the RWAs, other wheels must accommodate for the torque contribution loss, but in doing so can become saturated and lose of the system. As can be noted from results, the EKF estimation errors are the highest on average, with the SIF performing better. As noted previously, each respective filter will perform better for their designed use case. The NIS EKF-ESIF method, however, performed the best overall, where the difference in errors between the two are small. The switching mode was demonstrated to be much more consistent than the previously studied case of effectiveness loss, where the fault state is near constant for the fault duration. As before, there is a slight lag in realizing the fault, typically on the order of 5 seconds, due to the accumulation of the attitude error. Additionally, instead of predicting a non-faulty state prematurely, the NIS methods in the failure case adopt the SIF gain for almost 10 seconds after the fault ends. The slowly decaying behaviour of the NIS method can be specifically realized as beneficial for this failure case, as when power is restored the wheels can still be saturated and the system is not immediately operating as it should be.

Table 4: Reaction Wheel Failure Fault Case

RMSE $\times 10^{-3}$	EKF	SIF	WA NIS	FM NIS
$q_1$	0.01820	0.04837	0.03109	0.03134
$q_2$	0.02783	0.03974	0.03433	0.03457
$q_3$	0.04203	0.04103	0.02494	0.02464
$q_4$	0.01717	0.03955	0.027708	0.02831
$\omega_1$	0.83490	0.91827	0.68726	0.67307
$\omega_2$	0.55968	0.99352	0.77737	0.77435
$\omega_3$	1.49647	0.80760	0.70320	0.63705
$\Sigma_{RMSE}$	<b>2.99629</b>	<b>2.88808</b>	<b>2.28589</b>	<b>2.20333</b>



(a) Windowed Average NIS

(b) Fading Memory NIS

Figure 9: Sample NIS Plots for Hybrid EKF-SIF in Reaction Wheel Failure Case

## 6. CONCLUSION

In this paper, the adaptive NIS based EKF-ESIF was applied to a nonlinear satellite systems for robust estimation and fault detection for the first time. Background was provided considering the importance of attitude control and estimation, robust estimation strategies, and the consequences of faults on these systems. The satellite dynamic model was outlined for the simulator under study, along with the proposed estimation strategy. Two mechanisms for smoothing the NIS value were applied, where the NIS represents the consistency between the KF, and the innovation and its covariance.

The novel application of the NIS EKF-ESIF was validated using data obtained from an experimental CubeSat setup. The EKF, standard ESIF, and two adaptive NIS-based EKF-ESIF strategies were compared against each other by metric of RMSE in four operation modes. The four operating modes were the no fault, planar disturbance fault, and RWA effectiveness and functionality loss faults. For the ideal case, the proposed adaptive method was demonstrated to perform just as well as the EKF. In the fault cases, they exhibited superior performance over the EKF and SIF methods by themselves, able to switch gains based on the situation. The performance of the studied estimation strategies was averaged over the entire trial, and should be noted that in faulty events, the SIF performs better, where in normal operation the EKF is superior. Applying the adaptive switching strategy, we are able to detect when faults occur and utilize the most accurate estimation method in either case. Comparing the two methods of evaluating and smoothing the NIS, the fading memory generally resulted in higher accuracy over the windowed average. This was due to the retention of mild stochasticity in the windowed average, which resulted in falsely evaluating a faulty state as non-faulty. Alternatively, the fading memory method generally showed gradual decay in its values, typically having higher on times. Tuning the window size would likely solve

this issue.

The NIS-based method presented in this paper was validated as a superior and computationally light estimation strategy. For large faults, it is very effective, though less so for smaller faults that are harder to detect, like actuator effectiveness loss. The proposed method would likely be surpassed with a more informed fault identification method such as a neural network, at the cost of computation resources. A more robust fault identifier coupled with the gain switching method could be an avenue for future research. Downsides of applying the NIS method are involved in threshold and parameter tuning, which depend on the application and expected disturbance frequency. Additionally, the applicability of the NIS method for other faults could be explored, such as in a satellite system that experiences delays or packet loss due to cyber attacks.

## REFERENCES

- [1] Li, L., Yuan, L., Wang, L., Zheng, R., Wu, Y., and Wang, X., “Recent advances in precision measurement & pointing control of spacecraft,” *Chinese Journal of Aeronautics* **34**(10), 191–209 (2021). doi: [10.1016/j.cja.2020.11.018](https://doi.org/10.1016/j.cja.2020.11.018).
- [2] Yoshida, N., Takahara, O., and Kodeki, K., “Spacecraft with very high pointing stability: Experiences and lessons learned,” *19th IFAC Symposium on Automatic Control in Aerospace* **46**(19), 547–552 (2013). doi: [10.3182/20130902-5-DE-2040.00144](https://doi.org/10.3182/20130902-5-DE-2040.00144).
- [3] Jacklin, S. A., “Small-satellite mission failure rates,” tech. rep., National Aeronautics and Space Administration (2019).
- [4] Galvan, D. A., Hemenway, B., IV, W. W., and Baiocchi, D., [*Satellite Anomalies: Benefits of a Centralized Anomaly Database and Methods for Securely Sharing Information Among Satellite Operators*], RAND Corporation, Santa Monica, CA (2014).
- [5] Bedingfield, K. L. and Leach, R. D., [*Spacecraft system failures and anomalies attributed to the natural space environment*], vol. 1390, National Aeronautics and Space Administration, Marshall Space Flight Center (1996).
- [6] Lam, H.-L., Boteler, D. H., Burlton, B., and Evans, J., “Anik-E1 and E2 satellite failures of January 1994 revisited,” *Space Weather* **10**(10) (2012). doi: [10.1029/2012SW000811](https://doi.org/10.1029/2012SW000811).
- [7] Aeronautics, N. and Administration, S., “RPI Anomalous Events,” (2014). Accessed March 12, 2024.
- [8] Council, N. R. et al., [*Limiting future collision risk to spacecraft: an assessment of NASA’s meteoroid and orbital debris programs*], National Academies Press (2011).
- [9] Iannotta, B., “U.S. Satellite Destroyed in Space Collision,” (2009). Accessed March 12, 2024.
- [10] Inskeep, S., “NASA loses contact with Voyager Two after a programming error on Earth,” (2023). Accessed March 12, 2024.
- [11] Halans, J.-J., “Viasat Ukraine Case Study,” (2022).
- [12] Gonzaga, S. and et al., [*Hubble Space Telescope Primer for Cycle 21*], Space Telescope Science Institute (2012). Provided by the SAO/NASA Astrophysics Data System.
- [13] Wall, M., “‘Vibration Disturbance’ caused failure of new indian rocket, ISRO says,” (2023). Accessed March 12, 2024.
- [14] Xie, L. and Soh, Y. C., “Robust kalman filtering for uncertain systems,” *Systems & Control Letters* **22**(2), 123–129 (1994).
- [15] Berman, N. and Shaked, U., “H-infinity filtering for nonlinear stochastic systems,” in [*Proceedings of the 2005 IEEE International Symposium on, Mediterrean Conference on Control and Automation Intelligent Control, 2005.*], 749–754 (2005).
- [16] Li, W. and Jia, Y., “H-infinity filtering for a class of nonlinear discrete-time systems based on unscented transform,” *Signal Processing* **90**(12), 3301–3307 (2010).
- [17] Wang, Q., Li, J., Zhang, M., and Yang, C., “H-infinity filter based particle filter for maneuvering target tracking,” *Progress In Electromagnetics Research B* **30**, 103–116 (2011).
- [18] Habibi, S., “The smooth variable structure filter,” *Proceedings of the IEEE* **95**(5), 1026–1059 (2007).
- [19] Yan, X.-G. and Edwards, C., “Nonlinear robust fault reconstruction and estimation using a sliding mode observer,” *Automatica* **43**(9), 1605–1614 (2007).

- [20] Gadsden, S. A. and Al-Shabi, M., “The sliding innovation filter,” *IEEE Access* **8**, 96129–96138 (2020). doi: [10.1109/ACCESS.2020.2995345](https://doi.org/10.1109/ACCESS.2020.2995345).
- [21] Al-Shabi, M., Gadsden, S., and Habibi, S., “Kalman filtering strategies utilizing the chattering effects of the smooth variable structure filter,” *Signal Processing* **93**(2), 420–431 (2013).
- [22] Gadsden, S. A. and Habibi, S. R., “A new form of the smooth variable structure filter with a covariance derivation,” in [*49th IEEE Conference on Decision and Control (CDC)*], 7389–7394 (2010).
- [23] Gadsden, S. A. and Lee, A. S., “Advances of the smooth variable structure filter: square-root and two-pass formulations,” *Journal of Applied Remote Sensing* **11**(1), 015018 (2017).
- [24] Goodman, J., Hilal, W., Gadsden, S. A., and Eggleton, C. D., “Adaptive svssf-kf estimation strategies based on the normalized innovation square metric and imm strategy,” *Results in Engineering* **16**, 100785 (2022). doi: [10.1016/j.rineng.2022.100785](https://doi.org/10.1016/j.rineng.2022.100785).
- [25] Gadsden, S. A. and Kirubarajan, T., “Development of a variable structure-based fault detection and diagnosis strategy applied to an electromechanical system,” in [*Signal Processing, Sensor/Information Fusion, and Target Recognition XXVI*], Kadar, I., ed., **10200**, 102001E, International Society for Optics and Photonics, SPIE (2017).
- [26] Lee, A. S., Wu, Y., Gadsden, S. A., and AlShabi, M., “Interacting multiple model estimators for fault detection in a magnetorheological damper,” *Sensors* **24**(1) (2024).
- [27] Alsadi, N., Hilal, W., Gadsden, S. A., and Al-Shabi, M., “Derivation of the sliding innovation information filter for target tracking,” in [*Signal Processing, Sensor/Information Fusion, and Target Recognition XXXII*], Kadar, I., Blasch, E. P., and Grewe, L. L., eds., **12547**, 1254708, International Society for Optics and Photonics, SPIE (2023).
- [28] Lee, A. S., Hilal, W., Andrew Gadsden, S., and Al-Shabi, M., “Combined kalman and sliding innovation filtering: An adaptive estimation strategy,” *Measurement* **218**, 113228 (2023).
- [29] Hilal, W., Alsadi, N., Gadsden, S. A., and AlShabi, M., “An adaptive SIF and KF estimation strategy for fault detection based on the NIS metric,” in [*Society of Photo-Optical Instrumentation Engineers (SPIE) Conference Series*], *Society of Photo-Optical Instrumentation Engineers (SPIE) Conference Series* **12546**, 125460S (June 2023). doi: [10.1117/12.2664054](https://doi.org/10.1117/12.2664054).
- [30] Markley, F. L. and Crassidis, J. L., [*Fundamentals of spacecraft attitude determination and control*], vol. 1286, Springer (2014).
- [31] Kalman, R. E., “A new approach to linear filtering and prediction problems,” *Transactions of the ASME—Journal of Basic Engineering* **82**(Series D), 35–45 (1960).
- [32] Lee, A. S., Gadsden, S. A., and Al-Shabi, M., “An adaptive formulation of the sliding innovation filter,” *IEEE Signal Processing Letters* **28**, 1295–1299 (2021). doi: [10.1109/LSP.2021.3089918](https://doi.org/10.1109/LSP.2021.3089918).
- [33] Bar-Shalom, Y., Li, X. R., and Kirubarajan, T., [*Adaptive Estimation and Maneuvering Targets*], ch. 11, 421–490, John Wiley & Sons, Ltd (2001). doi: [10.1002/0471221279.ch11](https://doi.org/10.1002/0471221279.ch11).